



Deposited via The University of Sheffield.

White Rose Research Online URL for this paper:

<https://eprints.whiterose.ac.uk/id/eprint/100047/>

Version: Accepted Version

Article:

Exell , J.C., Thompson , M.J., Finger, L.D. et al. (2016) Cellular Active N-Hydroxyurea FEN1 Inhibitors Block Substrate Entry to the Active Site. *Nature Chemical Biology*, 12. pp. 815-821. ISSN: 1552-4450

<https://doi.org/10.1038/nchembio.2148>

Reuse

Items deposited in White Rose Research Online are protected by copyright, with all rights reserved unless indicated otherwise. They may be downloaded and/or printed for private study, or other acts as permitted by national copyright laws. The publisher or other rights holders may allow further reproduction and re-use of the full text version. This is indicated by the licence information on the White Rose Research Online record for the item.

Takedown

If you consider content in White Rose Research Online to be in breach of UK law, please notify us by emailing eprints@whiterose.ac.uk including the URL of the record and the reason for the withdrawal request.

1
2 **Cellular Active N-Hydroxyurea FEN1 Inhibitors Block**
3 **Substrate Entry to the Active Site**
4
5

6 Jack C. Exell,^{1,6} Mark J. Thompson,¹ L. David Finger,¹ Steven J. Shaw,¹
7 Judit Debreczeni,² Thomas A. Ward,⁴ Claire McWhirter,² Catrine L. B.
8 Siöberg,⁵ Daniel Martinez Molina,⁵ W. Mark Abbott,² Clifford D. Jones,³
9 J. Willem M. Nissink,^{3,*} Stephen T. Durant^{4,*} and Jane A. Grasby.^{1,*}

10
11 ¹Centre for Chemical Biology, Department of Chemistry, Krebs Institute, University
12 of Sheffield, Sheffield, S3 7HF, UK
13

14 ²Discovery Sciences, Innovative Medicines and Early Development Biotech Unit,
15 AstraZeneca, Unit 310 (Darwin Building), Cambridge Science Park, Milton Road,
16 Cambridge, CB4 0WG, UK.
17

18 ³Chemistry, Oncology, Innovative Medicines and Early Development Biotech Unit,
19 AstraZeneca, Unit 310 (Darwin Building), Cambridge Science Park, Milton Road,
20 Cambridge, CB4 0WG, UK and Alderley Park, Cheshire, SK10 4TG, UK.
21

22 ⁴Bioscience, Oncology, Innovative Medicines and Early Development Biotech Unit,
23 CRUK Cambridge Institute, Robinson Way, Cambridge, CB2 0RE, UK; Alderley
24 Park, Cheshire, SK10 4TG, UK and AstraZeneca, Unit 310 (Darwin Building),
25 Cambridge Science Park, Milton Road, Cambridge, CB4 0WG, UK.
26

27 ⁵Pelago Bioscience AB, Nobels Väg 3, 17165, Sweden
28

29 ⁶Current address: Department of Microbiology and Molecular Genetics, University of
30 California, Davis, Briggs Hall, One Shields Ave, Davis, CA 95616-8665, US
31

32
33 *To whom correspondence should be addressed. E-mail: j.a.grasby@sheffield.ac.uk,
34 stephen.durant@astrazeneca.com or willem.nissink@astrazeneca.com.
35

36 **Abstract**

37 The structure-specific nuclease human flap endonuclease-1 (hFEN1) plays a key role in DNA
38 replication and repair and may be of interest as an oncology target. We present the first crystal
39 structure of inhibitor-bound hFEN1 and show a cyclic *N*-hydroxyurea bound in the active site
40 coordinated to two magnesium ions. Three such compounds had similar IC₅₀ values but
41 differed subtly in mode of action. One had comparable affinity for protein and protein-
42 substrate complex and prevented reaction by binding to active site catalytic metal ions,
43 blocking the unpairing of substrate DNA necessary for reaction. Other compounds were more
44 competitive with substrate. Cellular thermal shift data showed engagement of both inhibitor
45 types with hFEN1 in cells with activation of the DNA damage response evident upon
46 treatment. However, cellular EC₅₀s were significantly higher than *in vitro* inhibition constants
47 and the implications of this for exploitation of hFEN1 as a drug target are discussed.

48

49

50 **Introduction**

51 Flap endonuclease 1 (FEN1) is the prototypical member of the 5'-nuclease superfamily,^{1,2}
52 whose activities span a range of cellular pathways involved in DNA replication and genome
53 maintenance.^{3,4} FEN1 is a structure-selective metallonuclease essential for Okazaki fragment
54 maturation through efficient removal of 5'-flaps resulting from strand displacement during
55 lagging-strand synthesis.^{5,6} This reaction produces nicked DNA suitable for ligation, thereby
56 ensuring maintenance of genomic fidelity. FEN1 is also involved in long-patch base excision
57 repair⁷⁻⁹ (LP-BER), amongst other pathways.

58

59 Given its critical replicative function, it is not surprising that FEN1 overexpression is
60 characterized in multiple cancer types¹⁰⁻¹³ such that it has been suggested as both a biomarker
61 relating to prognosis and disease progression, and a potential therapeutic target. Target
62 validation studies have focused either on chemosensitization^{14,15} or synthetic lethal
63 interactions¹⁶⁻¹⁹ with established oncogenes. Synthetic lethality arises when loss of function of
64 either gene of an interacting pair is not cytotoxic, but mutation or inhibition of both does
65 cause cell death; hence, targeting interacting partners of mutated genes in cancer offers
66 potential for selective killing of cancer cells.

67

68 Therapeutic interest in FEN1 arises from its known synthetic lethal interactions with several
69 genes frequently mutated in cancers.^{16,17,20} FEN1 inhibition selectively impairs proliferation of
70 colon cancer cells deficient in *Cdc4* and *Mre11a*,^{16,18} both frequently mutated in colorectal
71 cancers. FEN1 has also emerged as a potential chemosensitizing target due to its role in LP-
72 BER¹⁷ since it is critical for repair of MMS (methyl methanesulfonate)-induced alkylation
73 damage,²¹ and its knockdown or inhibition increases sensitivity to TMZ (temozolomide) in
74 glioblastoma¹³ and colorectal cancer^{14,16,18} cell lines.

75

76 This considerable interest in human FEN1 (hFEN1) as a drug target has prompted
77 development of high-throughput screening procedures^{22,23} and the discovery of an *N*-

78 hydroxyurea based series of hFEN1 inhibitors.²⁴ We investigated the specificity and mode of
79 action of these compounds and found they prevented access of the scissile phosphate diester
80 of substrate DNA to catalytic metal ions. We also demonstrated cellular activity and target
81 engagement in live cells, leading to activation of the DNA damage response and apoptosis.

82

83 **Results**

84 *N-Hydroxyurea hFEN1 inhibitors bind catalytic site metals*

85 Inhibitor **1**²⁴ (Figure 1a) was co-crystallized with hFEN1–Mg²⁺ truncated after residue 336
86 (hFEN1-336Δ), which retains all catalytic features but lacks the flexible 44 amino acid
87 C-terminus.^{25,26} The crystal structure of the hFEN1-336Δ–inhibitor complex (Figure 1b) was
88 solved at 2.84 Å resolution (Supplementary Results, Supplementary Table 1 and
89 Supplementary Figure 1; PDB ID 5FV7) and resembled a kidney bean with the active site and
90 requisite divalent metal ions residing at the indentation. The structure in the presence of the
91 active site-bound inhibitor closely resembled that of hFEN1 in complex with proliferating cell
92 nuclear antigen (PCNA).²⁷ As with the PCNA-bound structure, no density was observed for
93 the helical arch (α 4 and α 5) and α 2– α 3 loop regions, which are visible when co-crystallized
94 with substrate or product DNA.²

95

96 The inhibitor was situated in the protein's nuclease active site with the *N*-hydroxyurea moiety
97 directly coordinating two Mg²⁺ ions positioned 4.5 Å apart (Figure 1b), anchored by inner-
98 sphere metal-coordinating contacts from carboxylates of E160, D179 and D181 and outer-
99 sphere or water-mediated contacts from D34, D86, E158 and D233 (Figure 1c). The
100 thiophene ring of the inhibitor filled a small hydrophobic pocket formed by M37, Y40 and
101 V133, and the sulfur of M37 exhibited a short-distance (4Å) favorable contact to the electron
102 deficient pyrimidine-2,4-dione ring of the ligand. The 2,3-dihydrobenzo[*b*][1,4]dioxine
103 sidechain contacted M37 and Y40, though these contacts were less directional and mostly
104 hydrophobic in nature. It was evident that different binding poses in the active site are

105 possible for the *N*-hydroxyurea series of inhibitors, which goes some way to rationalizing the
106 reported SAR.²⁴ The relatively weak nature of protein contacts with the sidechain (N1-
107 substituent) explained the modest improvement in IC₅₀ values seen for compounds modified
108 at this position.²⁴ It is also understandable how substitutions restricting the conformational
109 freedom of the sidechain—for example, introduction of a methyl group at the 7-position of
110 the thieno[3,2-*d*]pyrimidine-2,4-dione system of **1**—would significantly reduce binding
111 affinity and therefore increase IC₅₀, as is reported.²⁴

112

113 *Inhibitor binding pose suggests a possible mode-of-action*

114 Coordination of **1** to the metal ions that catalyze specific phosphodiester hydrolysis of the
115 substrate suggested a mode of action for this inhibitor. We modelled ternary protein-
116 inhibitor-DNA complexes using the present hFEN1-336Δ-inhibitor structure together with
117 the published hFEN1-336Δ-product DNA complex² (Figure 1d). Alignment of product-bound
118 and ligand-bound structures indicated that the inhibitor and the phosphate monoester of the
119 product DNA strand both co-locate to bind the metal ions. Conversely, in the hFEN1-336Δ-
120 substrate DNA complex², the scissile bond is not in contact with active site metal ions
121 because the DNA is base-paired. It is assumed a pre-reactive complex forms initially that
122 requires the end of the DNA duplex to unpair and bind to metal ions as a prerequisite for
123 cleavage.^{1,2,28} Hence, it was considered plausible that substrate could bind in the presence of
124 inhibitor, but that this prevents DNA from accessing the catalytic metals as required for
125 hydrolysis to occur (Figure 2a). An alternative hypothesis was that the inhibitor precludes
126 DNA binding, although the compound was bound far from the other two main areas of
127 protein-DNA interaction (K⁺/H2TH motif and 3'-flap binding pocket). We undertook further
128 work to characterize the hFEN1-inhibitor interaction and establish whether the *N*-hydroxyurea
129 inhibitors compete with substrate DNA binding.

130

131

132 *Inhibitor binding to hFEN1 requires magnesium ions*

133 We quantified the interaction of **1**, and related analogs **2** and **3**²² bearing a smaller or no
134 sidechain (Figure 1a), with the substrate-free protein using isothermal titration calorimetry
135 (ITC; Supplementary Table 2). Similar dissociation constants (K_D) were obtained for **1** and **2**
136 in the presence of Mg^{2+} with either hFEN1-336 Δ (Supplementary Figure 2) or full-length
137 hFEN1 (Supplementary Figure 3a,b) but the K_D of **3** was approximately 10-fold higher,
138 suggesting interactions between the sidechains of **1** and **2** and the protein contribute to
139 binding.

140

141 Ca^{2+} ions are often employed as a nonviable cofactor in biophysical measurements with
142 hFEN1 because they facilitate accommodation of the substrate DNA and its required
143 conformational changes,^{28,29} but do not support catalysis. In fact, Ca^{2+} ions are a competitive
144 inhibitor of 5'-nuclease reactions with respect to Mg^{2+} ,^{30,31} implying both ions occupy similar
145 sites on the protein. However, K_D values were drastically increased on replacement of Mg^{2+}
146 with Ca^{2+} (Supplementary Figure 4), showing the latter did not support inhibitor binding.
147 Thus, in accord with the crystal structure, interaction of **1** and **2** with hFEN1 was specific to
148 the nuclease core domain and required Mg^{2+} . To provide an estimate of residence time, we
149 probed the interaction of **1** with hFEN1-336 Δ using surface plasmon resonance
150 (Supplementary Figure 2d) and obtained a dissociation constant similar to ITC with a
151 residence time of 3 min.

152

153 *Inhibitors bind to both protein and protein–DNA complex*

154 Kinetic experiments were used to characterize hFEN1 inhibition by **1**, **2** and **4**. We measured
155 rates of hFEN1-336 Δ -catalyzed reaction with an optimal endonucleolytic double-flap
156 substrate bearing a 5'-fluorescein label³² (DF1; Figure 2a, and Supplementary Figure 5a). At
157 substrate concentration close to K_M (100 nM), IC_{50} values for all three compounds were
158 similar (Table 1), and a related exonucleolytic substrate gave similar IC_{50} results

159 (Supplementary Figure 6a,b). Mode of inhibition was determined by globally fitting rates of
160 reaction at varying inhibitor and double-flap substrate concentrations to four inhibition
161 models: competitive, uncompetitive, non-competitive and mixed inhibition.

162

163 The uncompetitive model—where the inhibitor can only bind to enzyme–substrate complex—
164 afforded a poor fit for **1**, which was unsurprising given the compound’s high affinity for free
165 protein. The competitive model, where binding of inhibitor and substrate are mutually
166 exclusive, also proved unsuitable but the mixed and non-competitive models produced
167 acceptable fits (Figure 2b-d and Supplementary Figure 7). These models both assume the
168 inhibitor can bind to DNA-free and DNA-bound forms of the enzyme, but the non-
169 competitive model (Equation 4) assumes both complexes have equivalent ligand dissociation
170 constants. Allowing dissociation constants to vary (mixed inhibition; Figure 2b and Equation
171 5) produced a marginally better data fit, yielding near-equivalent dissociation constants for **1**
172 (Table 1). Statistical model selection using Aikake’s Information Criteria (AIC)
173 overwhelmingly preferred the mixed inhibition model.

174

175 With compound **2**, only the competitive (Equation 3) and mixed inhibition models produced
176 acceptable fits (Figures 2e, S8). The same statistical criteria (AIC) again favored the mixed
177 model, but in this case the derived dissociation constants (K_{ic} and K_{iu}) varied by an order of
178 magnitude (Table 1). For compound **4**, only the competitive model produced an acceptable fit
179 (Figure 2f, Table 1 and Supplementary Figure 9). Thus, whereas **1**, **2** and **4** all bound to
180 hFEN1–Mg²⁺ with similar efficiency, only **1** showed notable affinity for the enzyme-substrate
181 complex (hFEN1–Mg²⁺–DNA), binding both DNA-free and DNA-bound forms of the
182 enzyme with comparable dissociation constants.

183

184 *Evidence for an hFEN1–Mg²⁺–Inhibitor–DNA complex*

185 To verify formation of a quaternary complex of enzyme–Mg²⁺–inhibitor–DNA (E–Mg²⁺–I–
186 DNA), we tested the ability of E–Mg²⁺–I to form complexes with DNA without significant

187 hydrolysis of the substrate occurring. High concentrations of **1** or **2** (100 μ M) slowed the rate
188 of Mg^{2+} -catalyzed reaction 10,000-fold under single-turnover conditions (Table 1 and
189 Supplementary Figure 10), but appreciable substrate cleavage was still seen over the
190 timescale required for biophysical measurements. Because Ca^{2+} did not support inhibitor
191 binding (Supplementary Figure 4), substituting it in place of Mg^{2+} as a nonviable cofactor was
192 not applicable. Instead, we employed a previously characterized hFEN1 mutant, R100A.
193 Arg100 is strictly conserved in FEN1 proteins and its mutation to alanine slows reaction
194 7,000-fold.³³ The half-life of substrate with R100A- Mg^{2+} and inhibitors was sufficiently long
195 to permit measurements without significant product formation (Supplementary Figure 9), and
196 ITC confirmed the mutation did not affect inhibitor binding (Supplementary Table 2).

197

198 Both **1** and **2** formed R100A- Mg^{2+} -I-DNA complexes as demonstrated by increases in
199 anisotropy (r) of DF1 substrate upon titration with R100A- Mg^{2+} -I, with r reaching a common
200 limiting value at high enzyme concentration (Figure 3a). Data fitting to a simple binding
201 isotherm revealed similar trends in K_D between R100A and its wt equivalent, with which the
202 use of non-catalytic Ca^{2+} ions was necessary to prevent reaction (Supplementary Figures 11a-
203 d, 12a). Competing away bound, FAM-labeled substrate with its unlabeled equivalent
204 demonstrated specific interaction between R100A and this substrate (Supplementary Figures
205 5a,b, 11h). Substrate dissociation constants differed between quaternary complexes containing
206 **1** or **2** (Figure 3a): with compound **1**, R100A- Mg^{2+} -**1** displayed a K_D only threefold greater
207 than that for R100A- Ca^{2+} . In contrast, the substrate bound 10-fold more weakly to R100A-
208 Mg^{2+} -**2**. These results were consistent with **1** having a closer K_{iu} value relative to K_{ic} than **2**,
209 again suggesting **2** was more competitive than mixed in character.

210

211 *DNA is bent in complexes with or without inhibitors*

212 hFEN1 possesses two juxtaposed double-stranded DNA binding sites that accommodate
213 double-flap substrate DNA in a conformation with a 100° bend at the junction. To ascertain

214 whether DNA bound similarly in the presence of inhibitor, we examined substrate bending
215 using FRET. We labelled double-flap substrate with a rhodamine-fluorescein dye pair on its
216 respective duplexes, and verified binding to hFEN1 produces an increase in FRET signal³⁴
217 (Figure 3b and Supplementary Figures 5c-f, 14). Titration of R100A–Ca²⁺ or R100A–Mg²⁺–**1**
218 into the labeled substrate produced comparable FRET efficiency start and end values (Figure
219 3b) confirming the enzyme had engaged both DNA binding sites with or without inhibitor.
220 The substrate K_D was raised by a factor of three in the presence of **1**, whereas substrate
221 binding was much weaker with **2** present (Figure 3b and Supplementary Table 3); hence,
222 these results mirrored those obtained earlier by fluorescence anisotropy.

223

224 *Inhibitors bound to catalytic metals block DNA unpairing*

225 Unpairing of the reacting substrate duplex, which places the target phosphodiester onto active
226 site metal ions, is a prerequisite for hFEN1-catalysed reaction one nucleotide into the double-
227 stranded DNA (Figure 2a).²⁸ This metal ion-dependent conformational change may be
228 monitored using substrates containing a tandem 2-aminopurine (2AP) exciton pair at the –1
229 and –2 positions of the 5'-flap strand (DF3, Supplementary Figure 5g) by measuring changes
230 in the low energy exciton-coupled CD spectrum resulting from the 2APs, usually in the
231 presence of Ca²⁺ to prevent reaction.²⁸

232

233 In adopting the reactive conformation, the +1 and –1 nucleotides are assumed to become
234 extrahelical whereas the –2 nucleotide remains base-paired. In the absence of active site
235 divalent ions (EDTA added), a strong maximum at 330 nm is observed from the R100A–
236 DNA complex, due to the exciton pair and consistent with substrate remaining base-paired.²⁸
237 With R100A–Ca²⁺–DNA, the DNA conformational change reverses the sign of the CD signal
238 producing a deep minimum at 310 nm (Figure 4a). In the presence of **1** or **2**, the measured CD
239 signal of R100A–Mg²⁺–**I**–DNA did not differ significantly from that observed for R100A–
240 DNA without divalent ions (Figure 4b,c), even though the DNA was assumed to be fully
241 bound under these conditions (10 μ M DNA, 12.5 μ M R100A). This demonstrated that the

242 inhibitors prevented substrate conformational rearrangements necessary for hydrolysis
243 (Supplementary Figure 15).

244

245 *N-Hydroxyurea FEN1 inhibitors also target EXO1*

246 FEN1 is the prototypical member of the structure-specific 5'-nuclease superfamily, also
247 comprising exonuclease 1 (EXO1), gap endonuclease 1 (GEN1) and Xeroderma
248 Pigmentosum complementation group G protein (XPG).¹ Exoribonucleases XRN1 and 2 are
249 also suggested members of the superfamily.¹ These nucleases all share a similarly-folded
250 nuclease domain with similar active site geometry and full conservation of essential catalytic
251 residues.^{1,2} Consequently, it has been hypothesized that the substrate selectivity of these
252 proteins stems from strict recognition of their respective DNA substrate structures, followed
253 by double nucleotide unpairing to initiate scissile phosphate diester hydrolysis.¹

254

255 It is known that hFEN1 inhibitors can exhibit limited but manageable promiscuity towards
256 XPG.²⁴ However, testing against human EXO1-352Δ (nuclease domain of EXO1)³⁵ revealed
257 that compounds **1** and **2** both inhibited this target with IC₅₀ values similar to those against
258 hFEN1 (Supplementary Figures 5k, 6a,e). Differential scanning fluorimetry experiments³⁶
259 further confirmed binding of both compounds to both proteins in a divalent metal ion-
260 dependent manner (Supplementary Figure 6g,h). In contrast, inhibitor **1** was found ineffective
261 against bacteriophage T5 FEN (Supplementary Figures 5l, 6c) and *Kluyveromyces lactis*
262 XRN1 (Supplementary Figure 16), both of which show a high level of active site conservation
263 with the mammalian 5'-nuclease superfamily.¹ Similarly, **1** did not inhibit the structurally
264 unrelated DNA repair metallonuclease APE1 (Supplementary Figure 6f).

265

266 When hFEN1 acts *in vivo* it is usually associated with the toroidal clamp PCNA. PCNA
267 increases the stability of FEN1–DNA complexes,³⁴ suggesting that association with PCNA
268 might allow FEN1 to overcome inhibition. However, when we added hPCNA to hFEN1
269 reactions inhibited by **1** or **4**, the slow rates of reaction observed did not increase implying the

270 FEN1 interaction partner does not dramatically influence the IC₅₀ of either compound
271 (Supplementary Figure 6d).

272

273 *N-Hydroxyurea inhibitors engage with hFEN1 in live cells*

274 On the basis of contrasting inhibition modes, compounds **1** and **4** were selected for additional
275 cellular studies. We employed the cellular thermal shift assay technique (CETSA)³⁷ to
276 establish whether they interacted with hFEN1 in SW620 colon cancer cells. CETSA detects
277 changes in stability of a protein upon engagement with a ligand, like a biochemical thermal
278 shift assay, but is performed with whole cells and a target-specific, label-free readout of
279 engagement is obtained using a relevant antibody. Compounds **1** and **4** stabilized hFEN1
280 (Figure 5a-c and Supplementary Figure 17) with EC₅₀ = 5.1 μM and 6.8 μM, respectively, in
281 an isothermal concentration–response experiment, representing similar EC₅₀s regardless of
282 their differing modes of inhibition. Interestingly, these micromolar-range values represented a
283 substantial drop-off in observed binding affinity compared with observations in prior
284 biochemical assays (IC₅₀ = 46 nM and 17 nM, respectively; Table 1) so we undertook a
285 number of experiments to attempt to explain this. Cell permeability in MDCK and Caco-2
286 assays was not an issue (Supplementary Table 4); neither were other properties including
287 solubility and chemical stability. The compounds' affinity for free divalent metal ions in
288 solution was insignificant, ruling out metal chelation as an explanation. Nonspecific protein
289 binding may have contributed to the discrepancy between biochemical and phenotypic
290 potency, although binding to other 5'-nuclease superfamily members represented the most
291 obvious potential for off-target effects. Hence, we attempted further CETSA studies with **1**
292 and **4** against hEXO1 but this was concluded to be a non-viable CETSA target (with only
293 fragments of the protein detected on the blots), perhaps reflecting instability of the protein
294 under the assay conditions, or its cellular context as a component of multi-protein complexes
295 (which regulate its activity).

296

297

298 *hFEN1 inhibition activates the DNA damage checkpoint*

299 High concentrations of compound **1** proved cytotoxic towards SW620 cells with an EC₅₀ of
300 11 μM (Figure 5d), but HeLa cells stably expressing hFEN1-shRNA were 70% viable at 20
301 μM **1** (Figure 5e; purple curve). Mock-shRNA expressing HeLa cells were only 15% viable
302 under the same conditions (Figure 5e; black curve), showing similar susceptibility to **1** as
303 untransformed cells. Hence, a lack of hFEN1 conferred resistance to **1**, suggesting on-target
304 activity as the primary cause of cytotoxicity. SW620 cells also showed increased sensitivity to
305 MMS when co-treated with **1**, in a dose-dependent manner (Figure 5f), suggesting the
306 compound inhibits the LP-BER function of FEN1 in a cellular context. Enhanced toxicity of **1**
307 towards HeLa cells expressing *Rad54b*-shRNA (Figure 5e; green curve) was also observed
308 with an EC₅₀ of 6.4 μM compared to 14.9 μM against untransformed cells (Figure 5e,g),
309 confirming the synthetic lethal interaction between *Fen1* and *Rad54b* previously
310 demonstrated by silencing of the former.¹⁸ Inhibitor **4** also proved cytotoxic to HeLa cells
311 (EC₅₀ 6 μM; Figure 5g), appearing more potent than **1**, whose EC₅₀ of approximately 15 μM
312 was in line with its toxicity against SW620 cells.

313

314 When treated with sub-lethal doses of **1**, SW620 cells showed evidence of an induced DNA
315 damage response (Figure 5h and Supplementary Figure 18) at concentrations consistent with
316 the EC₅₀ for target engagement observed by CETSA. The same compound effected a dose-
317 dependent increase in ubiquitination of FANCD2, a marker for activation of the Fanconi
318 anemia pathway recruited to stabilize stalled replication forks.³⁸⁻⁴⁰ At higher doses,
319 accumulation of phosphorylated ATM and γH2AX was evident, indicating accumulation of
320 unrepaired DNA double-strand breaks (DSBs). Cells treated with high concentrations of **1**
321 also showed evidence of apoptosis, shown by the presence of cleaved PARP (Figure 5h).
322 Knockdown of hFEN1 by siRNA activated a similar DNA damage response to treatment with
323 **1**; these cells accumulated γH2AX but otherwise remained viable (Figure 5i and
324 Supplementary Figure 19). DNA damage response activation and apoptosis were consistent

325 with loss of hFEN1 function, because the consequences of unprocessed Okazaki fragments
326 would include stalled or collapsed replication forks, replication errors and double strand
327 breaks.

328

329 **Discussion**

330 *N*-Hydroxyurea compounds **1**, **2** and **4** prevented DNA cleavage with similar efficiency
331 (Table 1), reflecting the SAR observed previously for similar-sized compounds²⁴ inasmuch as
332 comparable IC₅₀ values were obtained despite notable differences in sidechain size and
333 structure. These results were consistent with protein–inhibitor binding mediated primarily
334 through interaction with active site Mg²⁺ ions, and a lack of strong contacts between the
335 protein and inhibitor sidechain, as seen in the structure of **1** bound to hFEN1 (Figure 1 and
336 Supplementary Table 2). Although the metal-coordinating headgroup clearly provided the
337 predominant binding contribution, the elevated *K*_D of **3** suggested interaction of the inhibitor
338 sidechain with the protein was nonetheless important for optimal affinity. Further studies
339 revealed subtle differences in mode of action on variation of the sidechain structure.

340

341 Although the DNA substrate bound in its usual conformation in the presence of compound **1**,
342 hydrolysis was impaired by prevention of double nucleotide unpairing through steric blocking
343 of the catalytic metals (Figures 1b-d, 3, 4). These observations were reminiscent of the action
344 of the HIV integrase inhibitor raltegravir.⁴¹ Raltegravir and functionally related compounds
345 bind to active site metal ions of the integrase–DNA complex, similarly obstructing access of
346 the reacting phosphodiester bond to the metals. In contrast, compounds **2** and **4**, with altered
347 sidechains, proved mostly competitive in character and primarily acted to reduce affinity of
348 the enzyme for its DNA substrate.

349

350 The micromolar EC₅₀s seen in CETSA experiments with **1** and **4** differed markedly from the
351 compounds' nanomolar potency against purified protein – though they were consistent with
352 phenotypic potency in DNA damage induction and cytotoxicity assays. A clear explanation

353 for this was not found, but the raised cellular EC₅₀s might reflect a high local concentration of
354 hFEN1 in the nucleus during S-phase, which could conceivably reach the micromolar range.
355 The residence time of compound **1** on hFEN1 proved similar to that of raltegravir on its target
356 (4.8 min),⁴² although this is short compared to the median of 51 min for a representative set of
357 marketed drugs,⁴² so the short residence time of **1** may necessitate a high local drug
358 concentration in the vicinity of the target for effective inhibition in cells.

359

360 Although hEXO1 is likely inhibited alongside hFEN1, the cellular concentration of hEXO1 is
361 not expected to be significantly higher, so this seems an unlikely explanation for the raised
362 EC₅₀ values. The results with hFEN1-deficient cells (Figure 5e) did suggest some degree of
363 target specificity, but previous cellular studies assuming selective inhibition of hFEN1 by the
364 *N*-hydroxyurea series must nonetheless be interpreted with caution based on the likelihood of
365 parallel hEXO1 inhibition, since it will not be possible to distinguish between phenotypes of
366 hFEN1 and hEXO1 inhibition with this class of compounds. One such published²⁴ inhibitor,
367 related to **1-4**, was employed to help validate a role for hFEN1 in homologous recombination
368 (HR),⁴³ demonstrating deficient HR upon treatment. However, hEXO1 is essential for
369 competent HR,⁴⁴⁻⁴⁷ and the observed phenotype is explicable by inhibition of this enzyme
370 alone. Although a role for hFEN1 in HR is otherwise supported in that study, we concluded
371 that the *N*-hydroxyurea series should not be regarded as exclusive hFEN1 inhibitors.

372

373 The mixed inhibition mode of **1**, which in theory permits ‘dead-end’ complexes of DNA and
374 protein to form, did not confer any advantageous inhibition characteristics in cells.
375 Unprocessed Okazaki fragments resulting from hFEN1 inhibition might be successfully
376 repaired by the cell with apoptosis only resulting when the DNA damage response is
377 overwhelmed. Some support for this notion was seen in SW620 cells treated with **1**, where we
378 observed dose-dependent activation of the Fanconi anemia pathway (Figure 5h). Because
379 FANCD2 is recruited to stabilize stalled replication forks and initiate repair,³⁸ treatment with
380 **1** evidently did interrupt replication, prompting cells to activate other pathways to repair

381 unprocessed Okazaki fragments directly. Failure to achieve this may cause collapse of
382 replication forks into DSBs, and at higher doses of compound **1**, we did see evidence for DSB
383 repair pathway activation. These markers did not accumulate at lower doses, so the damage
384 signal may only be obvious when the frequency of DSBs overwhelms the cell's DNA damage
385 response. Accumulation of cleaved PARP, indicating early apoptosis, also suggested cells
386 exposed to **1** were accumulating DNA damage associated with hFEN1 and/or hEXO1
387 inhibition and signaling for apoptosis.

388

389 Without exposure to inhibitor, both SW620 cells treated with hFEN1-siRNA and HeLa cells
390 stably expressing hFEN1-shRNA showed viability indistinguishable from untransformed
391 controls yet constitutively initiated a DNA damage response (Figure 5i). The hFEN1-shRNA
392 cells showed reduced sensitivity to **1**, suggesting a degree of selectivity and on-target activity
393 for the compound since the DNA damage response remained competent. Our data suggests
394 removal of functional hFEN1 alone did not induce toxicity and that damage associated with
395 its loss is successfully repaired until such mechanisms become overwhelmed. This result,
396 alongside our other observations in human cells, suggests targeting of hFEN1 in cancer will
397 not prove effective as a monotherapy, but could be useful in exploiting synthetic lethal
398 vulnerabilities. Synthetic lethal interactions between hFEN1 and *Rad54b*,¹⁸ *Cdc4*¹⁶ and
399 *Mre11a*¹⁶ are established, and other such interactions with potential clinical relevance are
400 proposed.^{16,38} We confirmed synthetic lethal interaction with *Rad54b*, previously established
401 using hFEN1 knockdown,¹⁸ through inhibition of the latter by **1**. Thus, hFEN1 inhibitors
402 might prove beneficial as a component of targeted or personalized therapies, provided
403 selectivity over hEXO1 and the other 5'-endonuclease superfamily members can be realized.

404

405 **Accession Codes**

406 The PDB accession code for the crystal structure presented in Figure 1 is 5FV7.

407

408 **Acknowledgements**

409 This work was supported by BBSRC grants BB/K009079/1 and BB/M00404X/1 (both to
410 JAG) and AstraZeneca. JCE thanks the EPSRC and AstraZeneca for a studentship. The
411 authors thank Dr Chris Phillips for assistance with submissions of the crystallographic data
412 and Dr Thomas McGuire for synthetic support.

413

414 **Author Contributions**

415 CJ designed and synthesized inhibitors, JCE, MJT, LDF and SJS carried out kinetic and
416 biophysical experiments. JCE, MJT, LDF, CM, JWMN, MA and JAG designed experiments
417 and analyzed this data. JD and JWMN obtained and analyzed structures. CLBS and DMM
418 performed the CETSA assays. TAW carried out other cellular experiments, and TAW and
419 STD analyzed data. All authors contributed to the preparation of the manuscript.

420

421 **Competing Financial Interest Statement**

422 MA, CM, JD, JWMN, TAW and STD are employees of AstraZeneca. CJ was an employee of
423 AstraZeneca at the time of writing. CLBS and DMM are employees of Pelago Bioscience AB.

424

425 **References**

426

- 427 1 Grasby, J. A., Finger, L. D., Tsutakawa, S. E., Atack, J. M. & Tainer, J. A. Unpairing
428 and gating: sequence-independent substrate recognition by FEN superfamily
429 nucleases. *Trends Biochem. Sci.* **37**, 74-84, doi:10.1016/j.tibs.2011.10.003 (2012).
- 430 2 Tsutakawa, S. E. *et al.* Human flap endonuclease structures, DNA double-base
431 flipping, and a unified understanding of the FEN1 superfamily. *Cell* **145**, 198-211,
432 doi:10.1016/j.cell.2011.03.004 (2011).
- 433 3 Kim, C. Y., Shen, B. H., Park, M. S. & Olah, G. A. Structural changes measured by
434 X-ray scattering from human flap endonuclease-1 complexed with Mg²⁺ and flap
435 DNA substrate. *J. Biol. Chem.* **274**, 1233-1239, doi:10.1074/jbc.274.3.1233 (1999).
- 436 4 Zheng, L. *et al.* Functional regulation of FEN1 nuclease and its link to cancer.
437 *Nucleic Acids Res.* **39**, 781-794, doi:10.1093/nar/gkq884 (2011).
- 438 5 Waga, S., Bauer, G. & Stillman, B. Reconstitution of complete SV40 SNA replication
439 with purified replication factors. *J. Biol. Chem.* **269**, 10923-10934 (1994).
- 440 6 Bambara, R. A., Murante, R. S. & Henricksen, L. A. Enzymes and reactions at the
441 eukaryotic DNA replication fork. *J. Biol. Chem.* **272**, 4647-4650 (1997).
- 442 7 Kim, K., Biade, S. & Matsumoto, Y. Involvement of flap endonuclease 1 in base
443 excision DNA repair. *J. Biol. Chem.* **273**, 8842-8848, doi:10.1074/jbc.273.15.8842
444 (1998).
- 445 8 Parikh, S. S., Mol, C. D., Hosfield, D. J. & Tainer, J. A. Envisioning the molecular
446 choreography of DNA base excision repair. *Curr. Opin. Struct. Biol.* **9**, 37-47,
447 doi:10.1016/s0959-440x(99)80006-2 (1999).

- 448 9 Beard, W. A. & Wilson, S. H. Structure and mechanism of DNA polymerase beta.
449 *Chem. Rev.* **106**, 361-382, doi:10.1021/cr0404904 (2006).
- 450 10 Mohan, V. & Srinivasan, M. in *New Research Directions in DNA Repair* (ed Clark
451 Chen) (InTech, 2013).
- 452 11 Singh, P. *et al.* Overexpression and hypomethylation of flap endonuclease 1 gene in
453 breast and other cancers. *Mol. Cancer Res.* **6**, 1710-1717, doi:10.1158/1541-
454 7786.mcr-08-0269 (2008).
- 455 12 Lam, J. S. *et al.* Flap endonuclease 1 is overexpressed in prostate cancer and is
456 associated with a high Gleason score. *BJU Int.* **98**, 445-451, doi:10.1111/j.1464-
457 410X.2006.06224.x (2006).
- 458 13 Nikolova, T., Christmann, M. & Kaina, B. FEN1 is overexpressed in testis, lung and
459 brain tumors. *Anticancer Res.* **29**, 2453-2459 (2009).
- 460 14 Panda, H. *et al.* Amino acid Asp181 of 5'-flap endonuclease 1 is a useful target for
461 chemotherapeutic development. *Biochemistry* **48**, 9952-9958, doi:10.1021/bi9010754
462 (2009).
- 463 15 Yoshimoto, K. *et al.* Complex DNA repair pathways as possible therapeutic targets to
464 overcome temozolomide resistance in glioblastoma. *Front. Oncol.* **2**, 186,
465 doi:10.3389/fonc.2012.00186 (2012).
- 466 16 van Pel, D. M. *et al.* An evolutionarily conserved synthetic lethal interaction network
467 identifies FEN1 as a broad-spectrum target for anticancer therapeutic development.
468 *PLoS Genet.* **9**, 11, doi:10.1371/journal.pgen.1003254 (2013).
- 469 17 Illuzzi, J. L. & Wilson, D. M. Base excision repair: contribution to tumorigenesis and
470 target in anticancer treatment paradigms. *Curr. Med. Chem.* **19**, 3922-3936 (2012).
- 471 18 McManus, K. J., Barrett, I. J., Nouhi, Y. & Hieter, P. Specific synthetic lethal killing
472 of RAD54B-deficient human colorectal cancer cells by FEN1 silencing. *Proc. Natl.*
473 *Acad. Sci. USA* **106**, 3276-3281, doi:10.1073/pnas.0813414106 (2009).
- 474 19 Durant, S. T. Telomerase-independent paths to immortality in predictable cancer
475 subtypes. *J. Canc.* **3**, 67-82, doi:10.7150/jca.3965 (2012).
- 476 20 Hwang, J.-C. *et al.* The overexpression of FEN1 and RAD54B may act as
477 independent prognostic factors of lung adenocarcinoma. *PLoS ONE* **10**, e0139435,
478 doi:10.1371/journal.pone.0139435 (2015).
- 479 21 Shibata, Y. & Nakamura, T. Defective flap endonuclease 1 activity in mammalian
480 cells is associated with impaired DNA repair and prolonged S phase delay. *J. Biol.*
481 *Chem.* **277**, 746-754, doi:10.1074/jbc.M109461200 (2002).
- 482 22 McWhirter, C. *et al.* Development of a high-throughput fluorescence polarization
483 DNA cleavage assay for the identification of FEN1 inhibitors. *J. Biomol. Screen.* **18**,
484 567-575, doi:10.1177/10870571113476551 (2013).
- 485 23 Dorjsuren, D., Kim, D., Maloney, D. J., Wilson, D. M. & Simeonov, A.
486 Complementary non-radioactive assays for investigation of human flap endonuclease
487 1 activity. *Nucleic Acids Res.* **39**, e11, doi:10.1093/nar/gkq1082 (2011).
- 488 24 Tumey, L. N. *et al.* The identification and optimization of a N-hydroxy urea series of
489 flap endonuclease 1 inhibitors. *Bioorg. Med. Chem. Lett.* **15**, 277-281,
490 doi:10.1016/j.bmcl.2004.10.086 (2005).
- 491 25 Finger, L. D. *et al.* The wonders of flap endonucleases: structure, function,
492 mechanism and regulation. *Sub. Cell Biochem.* **62**, 301-326, doi:10.1007/978-94-007-
493 4572-8_16 (2012).
- 494 26 Guo, Z. G. *et al.* Sequential posttranslational modifications program FEN1
495 degradation during cell-cycle progression. *Mol. Cell* **47**, 444-456,
496 doi:10.1016/j.molcel.2012.05.042 (2012).
- 497 27 Sakurai, S. *et al.* Structural basis for recruitment of human flap endonuclease 1 to
498 PCNA. *EMBO J.* **24**, 683-693, doi:10.1038/sj.emboj.7600519 (2005).
- 499 28 Finger, L. D. *et al.* Observation of unpaired substrate DNA in the flap endonuclease-1
500 active site. *Nucleic Acids Res.* **41**, 9839-9847, doi:10.1093/nar/gkt737 (2013).

501 29 Patel, N. *et al.* Flap endonucleases pass 5'-flaps through a flexible arch using a
502 disorder-thread-order mechanism to confer specificity for free 5'-ends. *Nucleic Acids*
503 *Res.* **40**, 4507-4519, doi:10.1093/nar/gks051 (2012).

504 30 Syson, K. *et al.* Three metal ions participate in the reaction catalyzed by T5 flap
505 endonuclease. *J. Biol. Chem.* **283**, 28741-28746, doi:10.1074/jbc.M801264200
506 (2008).

507 31 Tomlinson, C. G. *et al.* Neutralizing mutations of carboxylates that bind metal 2 in T5
508 flap endonuclease result in an enzyme that still requires two metal ions. *J. Biol.*
509 *Chem.* **286**, 30878-30887, doi:10.1074/jbc.M111.230391 (2011).

510 32 Finger, L. D. *et al.* The 3'-flap pocket of human flap endonuclease 1 is critical for
511 substrate binding and catalysis. *J. Biol. Chem.* **284**, 22184-22194 (2009).

512 33 Patel, N. *et al.* Proline scanning mutagenesis reveals a role for the flap endonuclease-
513 1 helical cap in substrate unpairing. *J. Biol. Chem.* **288**, 34239-34248,
514 doi:10.1074/jbc.M113.509489 (2013).

515 34 Craggs, T. D., Hutton, R. D., Brenlla, A., White, M. F. & Penedo, J. C. Single-
516 molecule characterization of Fen1 and Fen1/PCNA complexes acting on flap
517 substrates. *Nucleic Acids Res.* **42**, 1857-1872, doi:10.1093/nar/gkt1116 (2014).

518 35 Orans, J. *et al.* Structures of human exonuclease 1 DNA complexes suggest a unified
519 mechanism for nuclease family. *Cell* **145**, 212-223, doi:10.1016/j.cell.2011.03.005
520 (2011).

521 36 Niesen, F. H., Berglund, H. & Vedadi, M. The use of differential scanning
522 fluorimetry to detect ligand interactions that promote protein stability. *Nat. Protocol.*
523 **2**, 2212-2221 (2007).

524 37 Molina, D. M. *et al.* Monitoring drug target engagement in cells and tissues using the
525 cellular thermal shift assay. *Science* **341**, 84-87, doi:10.1126/science.1233606 (2013).

526 38 Moldovan, G.-L. & D'Andrea, A. D. How the fanconi anemia pathway guards the
527 genome. *Annu. Rev. Genet.* **43**, 223-249, doi:10.1146/annurev-genet-102108-134222
528 (2009).

529 39 Yeo, J. E., Lee, E. H., Hendrickson, E. A. & Sobeck, A. CtIP mediates replication
530 fork recovery in a FANCD2-regulated manner. *Hum. Mol. Genet.* **23**, 3695-3705,
531 doi:10.1093/hmg/ddu078 (2014).

532 40 Schlacher, K., Wu, H. & Jasin, M. A distinct replication fork protection pathway
533 connects Fanconi anemia tumor suppressors to RAD51-BRCA1/2. *Cancer Cell* **22**,
534 106-116, doi:10.1016/j.ccr.2012.05.015 (2012).

535 41 Di Santo, R. Inhibiting the HIV integration process: past, present, and the future. *J.*
536 *Med. Chem.* **57**, 539-566, doi:10.1021/jm400674a (2014).

537 42 Dahl, G. & Akerud, T. Pharmacokinetics and the drug-target residence time concept.
538 *Drug Discov. Today* **18**, 697-707, doi:10.1016/j.drudis.2013.02.010 (2013).

539 43 Fehrmann, R. S. N. *et al.* Gene expression analysis identifies global gene dosage
540 sensitivity in cancer. *Nat. Genet.* **47**, 115-125, doi:10.1038/ng.3173 (2015).

541 44 Bolderson, E. *et al.* Phosphorylation of Exo1 modulates homologous recombination
542 repair of DNA double-strand breaks. *Nucleic Acids Res.* **38**, 1821-1831,
543 doi:10.1093/nar/gkp1164 (2010).

544 45 Desai, A., Qing, Y. & Gerson, S. L. Exonuclease 1 is a critical mediator of survival
545 during DNA double strand break repair in non-quiescent hematopoietic stem and
546 progenitor cells. *Stem Cells* **32**, 582-593, doi:10.1002/stem.1596 (2014).

547 46 Tomimatsu, N. *et al.* Phosphorylation of EXO1 by CDKs 1 and 2 regulates DNA end
548 resection and repair pathway choice. *Nat. Comm.* **5**, doi:10.1038/ncomms4561
549 (2014).

550 47 Tomimatsu, N. *et al.* Exo1 plays a major role in DNA end resection in humans and
551 influences double-strand break repair and damage signaling decisions. *DNA Repair*
552 **11**, 441-448, doi:10.1016/j.dnarep.2012.01.006 (2012).

553

554 **Figure Legends**

555 **Figure 1. Compounds used in this study and crystal structure of hFEN1-336Δ in**

556 **complex with compound 1.** (a) Schematic illustration of compounds **1–4** that are inhibitors

557 of hFEN1 phosphate diester hydrolysis. (b) Structure of hFEN1-336Δ nuclease active site

558 (PDB ID 5FV7) showing the seven highly-conserved acidic residues (grey and red spheres

559 represent carbonyl carbon and oxygen atoms, respectively), the two bound magnesium ions

560 (pink spheres), and compound **1**. (c) Schematic representation of the metal-coordination

561 spheres of the two active site magnesium ions with distances reported in Ångstrom. (d)

562 Structure of hFEN1-336Δ in complex with product DNA (PDB ID 3Q8K) superimposed with

563 the hFEN1-336Δ in complex with compound **1** (protein not shown) to show that the inhibitor

564 and terminal nucleotide of the product DNA interact with the divalent magnesium ions and

565 share same pocket created by the protein. Metals are shown as pink spheres, terminal 5'

566 nucleotide (–1) highlighted in cyan box, penultimate nucleotide of the product DNA (–2)

567 highlighted in the pink box, and compound **1** highlighted in the green box.

568

569 **Figure 2. Differences in inhibition characteristics of the compounds.** (a) hFEN1-catalyzed

570 reaction schematic showing double nucleotide unpairing at positions +1 and –1 (numbering

571 relative to scissile phosphate). (b,c) Reaction schemes of mixed inhibition (b) and competitive

572 inhibition (c) models. In each case, E, S, I and P represent enzyme, substrate, inhibitor and

573 product, respectively. K_{ic} is the dissociation constant of I from free enzyme (competitive with

574 substrate) and K_{iu} is the dissociation constant of I from ES complex (uncompetitive). (d–f)

575 Nonlinear regression plots of normalized initial rates of reaction vs. substrate concentration

576 (open diamonds) for substrate DF1 at varying concentrations of compounds **1** (d; inset shows

577 equation for mixed inhibition model), **2** (e; inset shows legend correlating color/symbol to

578 inhibitor concentration) and **4** (f; inset shows equation for competitive inhibition model).

579 Error bars represent standard errors from global fitting of combined data from two triplicate

580 experiments (fits to alternative models are shown in Supplementary Figures S7–S9).

581

582 **Figure 3: Effect of inhibitors on substrate binding assessed by fluorescence anisotropy**

583 **(FA) and FRET.** (a) Typical FA titration data for hFEN1-R100A binding DF1 in the

584 presence of 10 mM Ca²⁺ (magenta, open triangles), 8 mM Mg²⁺ plus 100 μM compound **1**

585 (blue, open circles) or 8 mM Mg²⁺ with 100 μM compound **2** (green, open squares); three

586 independent titrations were carried out for all FA binding experiments. (b) Representative

587 curves of typical normalized FRET binding data for DF1 and hFEN1-R100A. Experiments

588 were conducted in triplicate, but only one data set and curve is shown here for each titration.

589 Colours and symbols for each of the three plots are the same as in panel (a).

590

591 **Figure 4: N-Hydroxyurea inhibitors prevent FEN1 reaction by blocking substrate**

592 **unpairing.** CD spectra recorded at pH 7.5 and 20 °C of (a) tandem 2-aminopurine containing

593 substrate DF3 (illustrated schematically as inset, and Supplementary Figure 5g) alone in the

594 presence of 10 mM Ca²⁺ (blue) or 25 mM EDTA (grey) and the same substrate bound to

595 hFEN1-R100A in the presence of 10 mM Ca²⁺ (magenta) or 25 mM EDTA (green); (b) DF3

596 bound to hFEN1-R100A in the presence of Mg²⁺ plus excess compound **1** (cyan) or EDTA

597 plus excess compound **1** (red); (c) DF3 bound to hFEN1-R100A with excess compound **2** in

598 the presence of Mg²⁺ (orange) or EDTA (purple). Full DNA sequences are shown in

599 Supplementary Tables 5,6 and Supplementary Figure 5g. Plots in panels a–c are

600 representative of experiments repeated independently three times.

601

602 **Figure 5. Cellular engagement and activity of hFEN1 inhibitors 1 and 4.** (a)

603 Representative data of Western blot intensities from a melt curve for compound **1** ((+)

604 indicates treated sample, (–) indicates control sample). (b) Melt and shift curve of FEN1 in

605 intact SW620 cells with 100 μM **1** (purple), **4** (orange) and DMSO (control, black). (c) Ratio

606 of hFEN1 protein isothermal shifts in cells with respect to concentration of compounds **1**

607 (purple) or **4** (orange) after exposure of cells to 50 °C to indicate magnitude of target

608 engagement of FEN1 in intact treated SW620 cells. (d) Dose-dependent sensitivity of SW620
609 cells to compound **1**. (e) Sensitivity of HeLa cells stably expressing *Fen1* (orange), *Rad54b*
610 (green) or non-targeting (black) shRNA to compound **1**. (f) MMS sensitivity of SW620 cells
611 treated with continuous dose of 10 μ M compound **1** (purple) or DMSO (control, black). (g)
612 Dose-dependent sensitivity of HeLa cells to compounds **1** and **4**. (h) Typical Western blots
613 showing **1** induces a DNA damage response in a dose-dependent manner. (i) SW620 cells are
614 insensitive to deletion of FEN1 by siRNA, but accumulate DNA damage. Panels (b) and (c)
615 show data from three independent triplicate experiments, fitted globally (i.e. N = 3, n = 9)
616 with standard error. Panels (d)–(g) and (i) show the mean of three independent experiments \pm
617 standard error.
618

619 **Tables**620 **Table 1.** Kinetic parameters in absence and presence of inhibitors.
621

Enzyme	Inhibitor	IC ₅₀ , nM [§]	<i>k_{cat}</i> , min ⁻¹	K _M , nM	K _{ic} , nM	K _{iu} , nM	<i>k_{STmax}</i> , min ⁻¹	t _{1/2} , min	ΔAIC _c
hFEN1	None	n.a.	165±9	20±3	n.a.	n.a.	916±49	7.57×10 ⁻⁴	n.a.
hFEN1	1	n.d.	n.d.	n.d.	n.d.	n.d.	0.48±0.04	1.43	n.a.
hFEN1	2	n.d.	n.d.	n.d.	n.d.	n.d.	1.52±0.09	0.46	n.a.
hFEN1-336Δ	None	n.a.	160±10	151±16	n.a.	n.a.	755±35	8.94×10 ⁻⁴	n.a.
hFEN1-336Δ	1	46.4±4.8	140±9	297±31	48±5	117±27	n.d.	n.d.	24.76*
hFEN1-336Δ	2	30.0±6.0	182±13	422±50	17±2	306±125	n.d.	n.d.	10.21 [¶]
hFEN1-R100A	None	n.a.	n.d.	n.d.	n.d.	n.d.	0.087±0.003	7.94	n.a.
hFEN1-R100A	1	n.d.	n.d.	n.d.	n.d.	n.d.	~4×10 ⁻⁴	≤1750	n.a.
hFEN1-R100A	2	n.d.	n.d.	n.d.	n.d.	n.d.	~2×10 ⁻³	≤360	n.a.
hFEN1-336Δ	4	16.9±1.2	194.5±11	630.8±53	26±2	n.a.	n.d.	n.d.	Amb.

622
623 [§]IC₅₀ values derived from rates at substrate concentration close to K_M (100 nM). *k_{STmax}* is
624 maximal reaction rate under single turnover conditions, used to calculate the substrate half-
625 life (t_{1/2}). ΔAIC_c is the difference between second order (corrected) Akaike Information
626 Criteria values between models; if ≥6, the likelihood the incorrect model was selected is P <
627 0.0001. ΔAIC_c for 1* and 2[¶] compares non-competitive with mixed-inhibition models and
628 competitive with mixed-inhibition models, respectively. Mixed-inhibition is preferred for
629 both. For 4, competitive inhibition was the only model whose fit was not ambiguous (Amb.).

630
631

632

633 **Online Methods**

634 ***Protein Expression and Purification***

635 ***hFEN1***-Wild-type hFEN1 and the mutant hFEN1 protein, R100A, were expressed from
636 previously-prepared pET28b vectors containing the appropriate sequences for WT or R100A
637 and subsequently purified and stored as described previously.² The C-terminally truncated
638 counterparts of wt-hFEN1 and R100A (i.e. hFEN1-Δ336 and R100A-Δ336 respectively) were
639 expressed from previously-prepared pET29b vectors containing the respective hFEN1-336
640 sequence in-frame with a PreScission protease site and (His)₆-tag after residue 336 (removing
641 44 residues). The proteins were then purified and stored as previously described.² T5FEN
642 protein was expressed and purified as previously described.²⁹

643

644 ***hEXO1***-To create a vector for the expression of truncated, wild-type hEXO1-352 bearing an
645 in-frame TEV protease site and C-terminal (His)₆-tag, primers (5'-
646 gtctctcccatgggatacagggtactac-3' and 5'-ggttctccccagctcttgaatgggcaggcatagc-3')—to amplify
647 hEXO1-352 DNA bearing leader sequences necessary for ligation independent cloning (LIC)
648 with SmaI-digested pMCSG28 vector (DNASU plasmid repository)—were utilized according
649 to protocol.⁴⁸ The DNA sequence encoding hEXO1-352-TEV-(His)₆-Stop was then subcloned
650 from the pMCSG28-hEXO1-352 vector into a pET21a vector using the NdeI and NotI
651 restriction sites with appropriate primers (5'-ggaattccatgggatacagggtactac-3' and 5'-
652 ggataagaatgcggccgcttaatgatgatgatggtgtgcc-3'). The hEXO1-352-TEV-(His)₆ protein was
653 expressed in BL21(DE3)-RIPL *E. coli* using autoinduction media as described. The protein
654 was purified by Co²⁺-immobilized affinity and anion exchange chromatography in a manner
655 analogous to that described previously for hFEN1.² Fractions containing hEXO1-352-TEV-
656 (His)₆ were pooled, concentrated using an Amicon ultrafiltration device with a 5,000 MWCO
657 membrane and then dialyzed into 2X 2L 50 mM Tris pH 7.0, 50 mM NaCl, 5 mM DTT, 1
658 mM EDTA, 5% glycerol containing 1000U of TurboTEV (BioVision) to remove the (His)₆-
659 tag. The dialysate was treated with MagneGST™ glutathione particles to remove the

660 TurboTEV, and then the protein was further purified using a Heparin affinity column and a
661 salt gradient from 0 to 1 M NaCl as described previously.³⁵ hEXO1-352-containing fractions
662 were pooled, concentrated by ultrafiltration as before and then applied to a 16/60 Sephacryl™
663 S-100 HR (GE Lifesciences) column. Fractions containing the protein were concentrated and
664 finally stored at 100 μM at -20 °C in 50 mM Tris pH 8.0, 50 mM NaCl, 1 mM DTT, 50 μM
665 EDTA, 50% v/v glycerol.

666

667 **PCNA**-The vector for human PCNA sub-cloned in-frame with a C-terminal-(His)₈-tag into
668 pET41b using the NdeI and XhoI restriction sites was a kind gift of Professor Binghui Shen
669 (Beckman Research Institute, City of Hope). The hPCNA-(His)₈ protein was expressed
670 overnight at 37 °C in BL21(DE3)-RIPL *E. coli* using autoinduction media as described.⁴⁹ The
671 cells were collected by centrifugation at 6000 g and resuspended in ice-cold PBS buffer. The
672 cells were pelleted again and the supernatant was removed. The cell pellet was resuspended in
673 Buffer A (25 mM Tris pH=7.4, 0.02% NaN₃, 5 mM imidazole, 2 mM β-mercaptoethanol)
674 containing 1M NaCl, 1X EDTA-free protease inhibitor cocktail, and 0.1 mg/mL lysozyme.
675 After cell lysis by freeze thaw and sonication, Buffer A containing 1% Tween-20 (10% of the
676 total volume of the lysate) was added. The lysate was clarified by centrifugation at 30,000 g
677 for 30 minutes at 4 °C. The supernatant was then applied to Co²⁺-TALON immobilized
678 affinity column and washed with 5 column volumes of Buffer A. The column was then
679 washed with 5 CV of Buffer A containing, 200 mM NaCl, and 0.01% NP-40. The protein was
680 then eluted in buffer B (25 mM Tris pH=7.4, 0.02% NaN₃, 200 mM NaCl, 250 mM
681 imidazole, 2 mM β-mercaptoethanol, 0.01% NP-40%). The eluate was directly applied to two
682 tandem 5 mL Hi-Trap Q columns and further purified as described.⁵⁰ Briefly, the fractions
683 containing hPCNA were pooled and dialysed 2 X 2L into Buffer C (25 mM KPO₄ pH=7.0,
684 0.01% NP-40%, 10% glycerol, 10 mM NaHSO₃, 5 mM DTT, 0.02% NaN₃). The dialysate
685 was passed through a 5 mL Hi-Trap S HP column that was pre-equilibrated with Buffer C to
686 remove impurities, but hPCNA was found exclusively in the flow-through. The flow-through

687 was loaded onto a hydroxylapatite column (BioSeptra HA Ultrogel, 11 cm by 2.6 cm) and then
688 eluted using a 20-column volume gradient from 0.025 and 0.5 M KPO₄ in Buffer C. The
689 eluate was dialysed 2 X 2Lt into Buffer D (25 mM potassium phosphate pH 7.0, 1.5 M
690 (NH₄)₂SO₄, 0.02% NaN₃). The dialysate was centrifuged at 3,300 g for 10 minutes at 4 °C to
691 remove any precipitate and then loaded onto a HiPrep Phenyl-Sepharose FF (high sub)
692 column and eluted using a 20 column volume inverse gradient using Buffer D and Buffer E
693 (25 mM potassium phosphate pH 7.0, 10% glycerol, 0.02% NaN₃). The isolated PCNA was
694 then dialysed into Buffer F (100 mM HEPES pH=7.5, 200 mM KCl, 10 mM DTT, 0.1 mM
695 EDTA, 0.04% NaN₃), and concentrated to provide 200 μM PCNA trimer (i.e. 600 μM
696 monomer) before the addition of glycerol to 50% v/v and storage at -20 °C.

697
698 **KIXRNI**-The vector corresponding to residues 1–1245 of *Kluyveromyces lactis* Xrn1 that was
699 subcloned in-frame with a C-terminal hexahistidine tag into pET-26b was a kind gift of
700 Professor Liang Tong laboratory (Columbia University). The protein was expressed in
701 Rosetta *E.coli* according to protocol⁵¹ and purified as described for hFEN1. Once purified, the
702 protein was stored in 20 mM Tris pH = 7.5, 200 mM NaCl, 2 mM DTT and 50% glycerol.
703 The purity of all proteins used was assessed by SDS-PAGE (Supplementary Figure 20).

704

705 **Crystallisation and Structure Determination** – The C-terminally truncated protein was
706 crystallized using the hanging drop vapor diffusion method. Briefly, the protein was
707 concentrated to approximately 8 mg/mL in a buffer containing 50 mM Tris pH 7.5, 200 mM
708 NaCl, 10 mM MgCl₂, 1 mM TCEP with 5 mM inhibitor **1** added. The crystallization well
709 contained 25% PEG 3350, 0.1 M MOPS pH 7.0, 5% 2-propanol and 2% glycerol. Crystals
710 appeared after 3 days at room temperature. Data were collected at the ERSF synchrotron on
711 station ID23 (T = 100 K). Data were processed and scaled using the XDS and SCALA
712 software packages.⁵² The crystals diffracted to 2.8 Å resolution, belong to Space Group P1
713 and having unit cell dimensions of $a = 43.3\text{Å}$, $b = 50.2\text{Å}$, $c = 66.9\text{Å}$, $\alpha = 102.1^\circ$, $\beta = 94.0^\circ$,
714 $\gamma = 90.7^\circ$. The structure was solved by molecular replacement, model rebuilding was

715 conducted using COOT⁵³ and the structure was refined using the BUSTER software.⁵⁴ The
716 final model has good geometry with 92% of residues in the favored region of the
717 Ramachandran plot, 7% in the allowed regions and 1% in the disallowed regions as defined
718 by PROCHECK.⁵² At convergence a final crystallographic R-factor of 23.3% was achieved.
719 Full data and refinement statistics are shown in Supplementary Table 1 and ligand electron
720 density in Supplementary Figure 1.

721

722 ***Isothermal Titration Calorimetry (ITC)*** – Binding affinities of wt hFEN1, hFEN1-336Δ and
723 hFEN1-R100A for compounds **1** and **2** were measured using either a VP-ITC
724 microcalorimeter (GE Healthcare) or NANO-ITC (TA Instruments). The appropriate protein
725 was exchanged from storage buffer into 100 mM KCl, 1 mM DTT, 50 mM HEPES pH 7.5
726 containing 8 mM MgCl₂ or 10 mM CaCl₂ using a HiPrep 26/10 desalting column at 4 °C.
727 Subsequently, the protein was dialyzed overnight at 4 °C against the same buffer composition.
728 In all cases, the dialysate was used prepare a solution with final protein concentration 18 μM
729 (based on A₂₈₀ using extinction coefficients calculated using the ExpASY ProtParam tool,
730 <http://web.expasy.org/protparam/>) and final inhibitor concentration 200 μM, diluted from
731 DMSO stock solution to a final DMSO concentration of 1%. Twenty-five injections were
732 performed with 180 s spacing time at 25 °C. Titration traces were integrated by NITPIC⁵⁵ and
733 the resultant curves were globally fit by SEDFIT.⁵⁶ The figures were prepared using GUSSI
734 (<http://biophysics.swmed.edu/MBR/software.html>).

735

736 ***Synthesis and Purification of DNA constructs*** – The DNA oligonucleotides detailed in
737 Supplementary Table 5, including those synthesised with 5'-fluorescein-CE-phosphoramidite
738 (6-FAM), internal dSpacer-CE-phosphoramidite (dS) or containing site-specific 2-
739 aminopurine (2AP) substitutions, were purchased with HPLC purification from DNA
740 Technology A/S (Risskov, Denmark). MALDI-TOF spectrometry confirmed experimental
741 molecular weights were all within 3 Da of calculated values (data not shown). The

742 concentration of individual oligonucleotides was determined by measuring the absorbance at
743 260 nm (20 °C), using an extinction coefficient (ϵ_{260}) calculated with OligoAnalyzer 3.1
744 (<https://eu.idtdna.com/calc/analyzer>). Heteroduplex substrates were prepared by heating the
745 appropriate flap (or exo) strand with the complementary template in a 10:11 ratio at 95 °C for
746 5 min in 100 mM KCl, 50 mM HEPES pH 7.5 with subsequent cooling to room temperature
747 (Supplementary Table 6 and Supplementary Figure 5).

748

749 **Steady-state kinetic experiments** – Reaction mixtures containing twelve different
750 concentrations of FAM-labeled DF1 (Supplementary Figure 5a) substrate were prepared in
751 reaction buffer (RB; 55 mM HEPES pH 7.5, 110 mM KCl, 80 mM MgCl₂, 0.1 mg/mL bovine
752 serum albumin, 1 mM DTT) and incubated at 37 °C for 10 min. Reactions were initiated by
753 the addition of hFEN1-336Δ in RB. Reactions were sampled at seven time intervals between
754 2–20 min and quenched with excess EDTA (250 mM) with reaction progress being monitored
755 by dHPLC equipped with a fluorescence detector (Wave[®] fragment analysis system,
756 Transgenomic UK) as described.³² All reactions were independently repeated four times.
757 Initial rates (v_0 , nM min⁻¹) were determined by linear regression of plots of the amount of
758 product concentration *versus* time up to 10% product formation. Kinetic parameters k_{cat} and
759 K_M were determined by generalized nonlinear least squares using a Michaelis–Menten model
760 (Equation 1), from plots of normalized initial rates ($v_0/[E]_0$, min⁻¹) as a function of substrate
761 concentration. The error distribution was assumed to be Gaussian, but to account for the
762 unequal variance with increasing substrate concentration the variance was weighted to $1/Y^2$.
763 All graph fitting and statistical analyses were done using GraphPad Prism 6.04 (GraphPad
764 Software, Inc.).

$$\frac{v_0}{[E]_0} = \frac{k_{cat}}{K_M + [S]} \quad \text{Equation 1}$$

766

767 **Inhibition Studies** – The steady-state kinetic parameters of hFEN1-336Δ with DF1 were
768 determined as above at various concentrations of **1**, **2** and **4** (0, 5, 10, 50, 100, 500, 1000 nM)

769 diluted from DMSO stock solutions as required. For each inhibitor concentration, reactions
770 were followed in triplicate (each replicate using an independent serial dilution of enzyme) at
771 six different concentrations of DF1 (10, 50, 100, 500, 1000, 5000 nM). Each experiment was
772 independently conducted twice in triplicate. RB was used with a final DMSO concentration of
773 1% (this DMSO concentration did not affect reaction rates in the absence of inhibitor).
774 Reactions were assayed, and normalized initial rates were determined, as described for
775 steady-state analyses. Kinetic parameters k_{cat} and K_M were determined globally for the four
776 simplest types of reversible linear inhibition: uncompetitive (Equation 2), competitive
777 (Equation 3), non-competitive (Equation 4) and mixed (Equation 5) by non-linear regression
778 plots of normalized initial rates ($v_o/[E]_o, \text{min}^{-1}$) *versus* the substrate concentration for each
779 concentration of inhibitor. The same weighting as above ($1/Y^2$) was applied in each case. In
780 addition to the goodness of fit of these calculated slopes to the raw normalized initial rates,
781 statistical analyses were done using GraphPad Prism. Akaike information criteria (AIC) was
782 employed as a statistical test to aid model selection (e.g. non-competitive *versus* competitive).
783 Unless the more complex model gave a difference in AIC of more than -6 (95% probability),
784 the less complex model was preferred as the appropriate one. This type of analysis penalizes
785 the more parameterized model unless the sum-of-squares is significantly reduced. As an
786 additional check, the residuals from both the non-competitive and mixed inhibition models
787 were inspected. IC_{50} values for inhibition of hFEN1-336 Δ by compounds **1**, **2** and **4** (reported
788 in Figure 2g) were derived from data obtained at 100 nM substrate DF1 and the same
789 concentrations of inhibitor as above, using nonlinear regression in GraphPad Prism.
790

$$\frac{v_0}{[E]_0} = \frac{k_{cat}[S]}{K_M + [S] \left(1 + \frac{[I]}{K_{iu}}\right)} \quad \text{Equation 2}$$

$$\frac{v_0}{[E]_0} = \frac{k_{cat}[S]}{K_M \left(1 + \frac{[I]}{K_{ic}}\right) + [S]} \quad \text{Equation 3}$$

$$\frac{v_0}{[E]_0} = \frac{k_{cat}[S]}{K_M \left(1 + \frac{[I]}{K_i}\right) + [S] \left(1 + \frac{[I]}{K_i}\right)} \quad \text{Equation 4}$$

$$\frac{v_0}{[E]_0} = \frac{k_{cat}[S]}{K_M \left(1 + \frac{[I]}{K_{ic}}\right) + [S] \left(1 + \frac{[I]}{K_{iu}}\right)} \quad \text{Equation 5}$$

799

800 The rates of reaction of hFEN1-, hFEN1-PCNA-, hEXO1- and T5FEN-catalysed reactions of
 801 SF, DF4, EO and pY7 (Supplementary Tables 5,6 and Supplementary Figure 5h,i),
 802 respectively, were also determined at varying concentrations of compounds **1** and **4** (hFEN1-
 803 PCNA), **1** and **2** (hEXO1) or **1** only (T5FEN) in an analogous fashion at fixed concentrations
 804 of substrate as detailed in Supplementary Figure 6b-e.

805

806 RNA and DNA oligonucleotides used in XRN1 assays were ordered purified using reverse-
 807 phase HPLC and synthesised by DNA Technology (Risskov, Denmark), using standard
 808 phosphoramidites. Reactions were performed as described,⁵¹ but were monitored by
 809 denaturing PAGE using a Chemidoc system (Bio-Rad) to visualize the FAM and TAMRA
 810 labelled oligos (Supplementary Figure 16).

811

812 Human APE1 was purchased from Sino Biologicals via Life Technologies. APE1 was
 813 assayed with the AP1 substrate⁵⁷ in 50 mM HEPES-KOH pH 7.5, 25 mM KCl, 5 mM MgCl₂
 814 and 0.1 mg/mL BSA. The reaction was monitored by dHPLC in a manner analogous to FEN1.

815

816 **Determination of k_{STmax} of hFEN1, hFEN1-336Δ and hFEN1-R100A in the presence and**
 817 **absence of inhibitors** – Maximal single turnover rates of reaction were determined using
 818 rapid quench apparatus, or manual sampling where appropriate, in triplicate (technical

819 replicates) at 37 °C as described.³² To initiate reaction, enzyme at a final concentration of at
820 least $10 \times K_d$ of the substrate (DF1; Supplementary Tables 56 and Supplementary Figure 5a)
821 in RB was added to an equal volume of substrate in the same buffer. To determine k_{STmax} in
822 the presence of the inhibitor **1** or **2**, reaction mixtures were prepared as above but containing
823 100 μ M (1% DMSO) of either inhibitor. Samples were quenched (1.5 M NaOH, 80 mM
824 EDTA) over a range of different time intervals and reaction progress monitored as above.³²
825 The first-order rate constant (k_{STmax}) of reaction was determined by plotting the appearance of
826 product against time (P_t) and applying nonlinear regression to Equation 6, where P_∞ is the
827 amount of product at endpoint.

828

829 $P_t = P_\infty (1 - \exp^{-k_{STmax}t})$ Equation 6

830

831 **Fluorescence Anisotropy** – Dissociation constants for free enzyme and the enzyme–inhibitor
832 complex with the DNA substrate (DF1; Supplementary Tables 5,6 and Supplementary Figure
833 5a) were measured under equilibrium conditions by fluorescence anisotropy using a Horiba
834 Jobin Yvon FluoroMax-3[®] spectrofluorometer with automatic polarizers. The excitation
835 wavelength was 490 nm (slit width 5 nm) with emission detected at 510 nm (slit width 5 nm).
836 Samples contained 10 mM CaCl₂ or 2 mM EDTA (or when inhibitors were present 8 mM
837 MgCl₂) and 10 nM DF1, 110 mM KCl, 55 mM HEPES pH 7.5, 0.1 mg/mL bovine serum
838 albumin, 1 mM DTT and 1% DMSO. Inhibitors **1** and **2** were added at 100 μ M as
839 appropriate. This solution containing substrate was incubated at 37 °C for a minimum of 10
840 min before the first measurement at 0 nM protein with subsequent readings taken on the
841 cumulative addition of enzyme in a matched buffer, with corrections made for dilution. Data
842 were modeled by nonlinear least squares regression in KaleidaGraph 4.0 using Equation 7,
843 where r is the measured anisotropy at a particular total concentration of enzyme ($[E]$) and
844 fluorescent substrate ($[S]$), with r_{min} giving the minimum anisotropy, of free DNA, and r_{max} the
845 maximum anisotropy, the anisotropy of the saturated substrate.

$$r = r_{\min} + \frac{(r_{\max} - r_{\min})}{2[S]} \left[([S] + [E] + K_D) - \sqrt{([S] + [E] + K_D)^2 - 4[S][E]} \right]$$

Equation 7

847 The equilibrium dissociation constant $K_{d(\text{binding})}$ is extracted from this analysis. Each
 848 measurement was independently repeated in triplicate (Supplementary Figure 10), and
 849 samples were taken after completion of the titration and analyzed by dHPLC to determine the
 850 amount of product produced (Supplementary Figure 11a).

851

852 **Fluorescence Anisotropy Competition Experiments** – Samples were prepared and anisotropy
 853 readings taken as described for the protein–DNA equilibrium binding measurements above.
 854 Enzyme was added cumulatively up to ~ 80% saturation of the substrate (DF1;
 855 Supplementary Tables 5,6 and Supplementary Figure 5a). At this point unlabeled DNA in the
 856 same buffer (DF2; Supplementary Table 5,6 and Supplementary Figure 5b) was added in a
 857 stepwise manner with readings taken after each addition of the competitor until the anisotropy
 858 value reached that of oligonucleotide in the absence of any protein (Supplementary Figure
 859 11h).

860

861 **Fluorescence Resonance Energy Transfer (FRET)** – FRET energy transfer efficiencies (E)
 862 were determined using the $(\text{ratio})_A$ method⁵⁸ by measuring the enhanced acceptor
 863 fluorescence. The steady state fluorescent spectra of 10 nM non-labeled trimolecular, donor-
 864 only labeled and doubly-labeled DNA substrates (Supplementary Figure 5c,d,f) were recorded
 865 using a Horiba Jobin Yvon FluoroMax-3[®] fluorometer and normalized for lamp and
 866 wavelength variations. For direct excitation of the donor (fluorescein, DOL) or acceptor
 867 (rhodamine, AOL; Supplementary Figure 5e), the sample was excited at 490 nm or 560 nm (2
 868 nm slit width) and the emission signal collected from 515–650 nm or 575–650 nm (5 nm slit
 869 width). Emission spectra were corrected for buffer and enzyme background signal by
 870 subtracting the signal from the non-labeled (NL) DNA sample. In addition to 10 nM of the
 871 appropriate DNA construct samples contained 10 mM CaCl₂ or when inhibitor was present 8

872 mM MgCl₂ or 2 mM EDTA and 110 mM KCl, 55 mM HEPES pH 7.5, 0.1 mg/mL bovine
 873 serum albumin, 1 mM DTT, 1% DMSO and 100 μM inhibitor **1** or **2** as appropriate. The first
 874 measurement was taken prior to the addition of protein (either hFEN1-WT or hFEN1-R100A)
 875 with subsequent readings taken on the cumulative addition of enzyme, with corrections made
 876 for dilution. Transfer efficiencies (E) were determined according to Equation 8, where F_{DA}
 877 and F_D represent the fluorescent signal of the doubly-labeled DNA (DAL) and donor-only-
 878 labeled DNA (DOL) at the given wavelengths, respectively; ε^D and ε^A are the molar
 879 absorption coefficients of donor and acceptor at the given wavelengths; and ε^D(490)/ε^A(560)
 880 and ε^A(490)/ε^A(560) are determined from the absorbance spectra of doubly-labeled molecules
 881 (DAL) and the excitation spectra of singly rhodamine-only-labeled molecules (AOL). Energy
 882 transfer efficiency (E) was fit by non-linear regression to Equation 9, where E_{min} and E_{max} are
 883 the minima and maxima of energy transfers, [S] is the substrate concentration, [P] is the
 884 protein concentration and K_D is the binding equilibrium dissociation constant of the protein
 885 substrate [PS] complex.

$$886 \quad (\text{ratio})_A = (F_{DA}(\lambda_{EX}^D, \lambda_{EM}^A) - N \cdot F_D(\lambda_{EX}^D, \lambda_{EM}^A)) / F_{DA}(\lambda_{EX}^A, \lambda_{EM}^A)$$

887

$$888 \quad N = F_{DA}(\lambda_{EX}^D, \lambda_{EM}^D) / F_D(\lambda_{EX}^D, \lambda_{EM}^D)$$

889

890

$$891 \quad \text{Equation 8} \quad E = (\text{ratio})_A / (\epsilon^D(490) / \epsilon^A(560)) - (\epsilon^A(490) / \epsilon^A(560))$$

$$892 \quad \text{Equation 9} \quad E = E_{\min} + \frac{(E_{\max} - E_{\min})}{2[S]} \left[([S] + [P] + K_D) - \sqrt{([S] + [P] + K_D)^2 - 4[S][P]} \right]$$

893

894 **2-Aminopurine Exciton-Coupled Circular Dichroism (ECCD) Spectroscopy** – Spectra were
 895 recorded of samples containing 10 μM DF3 (Supplementary Figure 5g), 110 mM KCl, 55
 896 mM HEPES pH 7.5, 1 mM DTT and either 10 mM CaCl₂; 10 mM CaCl₂ + 25 mM EDTA; 8
 897 mM MgCl₂ + 100 μM compound **1** or **2**; or 8 mM MgCl₂ + 100 μM compound **1** or **2** + 25
 898 mM EDTA; and, where appropriate, 12.5 μM protein, using a JASCO J-810 CD
 899 spectrophotometer (300–480 nm) at 20 °C as described.²⁸ In samples containing either

900 inhibitor **1** or **2**, the enzyme was pre-incubated with the inhibitor before addition of the
901 substrate. The CD spectra were plotted as $\Delta\epsilon$ per mol of 2AP residue versus wavelength. Each
902 measurement was independently repeated (typically in triplicate) and gave similar results.
903 After measurements were recorded aliquots were taken and the amount of product produced
904 was checked by dHPLC (Supplementary Figure 12b).

905

906 **Differential Scanning Fluorimetry (DSF)** – The stability of purified hFEN1 and hEXO1-352
907 with and without available Mg^{2+} was assessed as a function of inhibitor concentration by
908 DSF³⁶ using the fluorescent probe SYPRO[®] Orange (Sigma–Aldrich). Final volumes of 20 μ L
909 containing 2.5 μ M hFEN1 or hEXO1-352 in 50 mM HEPES–KOH pH 7.5, 100 mM KCl, 8
910 mM $MgCl_2$, 1 \times SYPRO[®] Orange with either 25 mM EDTA or 25 mM NaCl and various
911 concentrations of compound **1** or **2** (0, 1, 2, 4, 6, 8, 10, 20, 40, 60, 80, 100 μ M) were mixed in
912 white 96-well PCR-plates (Starlab) and sealed with StarSeal Advanced Polyolefin Film
913 (Starlab). The plates were inserted into an Agilent MX3005P QPCR instrument for thermal
914 denaturation. The emission at 610 nm (excitation 492 nm) from each well was recorded from
915 25 to 95 °C at a scan rate of 1 °C/min with a filter set gain multiplier of $\times 4$. Analysis of the
916 resulting thermal denaturation curves was accomplished using the DSF Analysis Excel³⁶
917 script as described (<ftp://ftp.sgc.ox.ac.uk/pub/biophysics>) in combination with GraphPad
918 Prism 6.04, which provided the nonlinear regression function with the Boltzman equation
919 (Equation 10).

920
$$I(x) = I_0 + \frac{I_1 - I_0}{1 + e^{\left(\frac{T_m - T(x)}{\text{slope}}\right)}} \text{ Equation 10}$$

921

922 **Cellular Thermal Shift Assay (CETSA)**

923 CETSA was performed as described³⁷ by first establishing melt curves and ligand-induced
924 shifts followed by testing of the compounds with increasing concentrations of **1** or **4** at a
925 single temperature to establish the CETSA EC_{50} of target engagement. Target engagement
926 was determined by isothermal concentration–response (IsoT C–R) stabilization curves for

927 compound **1** and **4** on hFEN1 in treated intact cells. Western blots were performed using an
928 iBlot2 device (Life Technologies) on nitrocellulose membranes. Transfer was set to 8 minutes
929 at 25 V. Blocking and dilution of antibodies were performed in 5% non-fat milk in Tris
930 Buffered Saline–Tween (TBST). A commercially available primary antibody against hFEN1
931 (ab109132, Abcam) was diluted at 1:5000 and incubated at 4 °C overnight. Specific hFEN1
932 bands were then detected using the horseradish peroxidase (HRP) conjugated secondary
933 antibody sc-2374 (Santa Cruz Biotechnology) together with Clarity Western ECL substrate
934 (BioRad).

935

936 Melt and shift curves (Figure 5a,b) for FEN1 in intact SW-620 cells were determined by
937 washing cells with HBSS followed by trypsinization using TrypLE (Gibco) and pelleting by
938 centrifugation. The pellet was washed with HBSS, pelleted and re-suspended in HBSS to a
939 cell density of 20 million cells/mL. Compound incubation was performed during 60 minutes
940 at 37 °C at 100 µM final concentration, whereas 0.2% DMSO was used as negative control.
941 The samples were gently mixed every 10 min. Cell viability was measured before and after
942 compound incubation. The treated cells were divided into 50 µL aliquots and subjected to a
943 12-step heat challenge between 37 and 70 °C for 3 min, followed by immediate cell lysis by 3
944 rounds of freeze–thawing. Precipitated protein was pelleted by centrifugation at 20,000 g for
945 20 min, then 30 µL of the supernatant was mixed with 15 µL gel loading buffer (NuPAGE
946 LDS sample buffer, Life Technologies) and 10 µL/lane of the mixture was loaded to a gel.
947 Protein amounts were detected using Western blot techniques as described above.

948

949 Isothermal concentration response curves (Figure 5c) were determined with intact SW-620
950 cells treated as above, but at a final concentration of 40 million cells/mL. The cell suspension
951 was divided into 30 µL aliquots and an equal volume of HBSS containing 2× the intended
952 compound concentration was added, resulting in a final cell concentration of 20 million
953 cells/mL at the correct concentration. A 7-step dilution concentration response series of the

954 ligands in 0.2% DMSO was applied together with 0.2% DMSO as control. The log₁₀ dilution
955 series ranged from 100 pM to 100 μM. An additional 7-step series was applied, ranging from
956 100 nM to 300 μM. The cells were incubated with ligand at 37 °C for 60 min, with gentle
957 mixing every 10 min. The aliquots were heated to a single specific temperature, 50 °C, as
958 determined from the previously established FEN1 melt and shift curves, for 3 min, and lysed
959 by 3 cycles of freeze–thawing. Precipitated protein and cellular debris were pelleted by
960 centrifugation at 20.000 g for 20 min then 40 μL of the supernatant was mixed with 20 μL
961 LDS sample buffer. Protein amounts were detected after loading 10 μL/lane of the
962 supernatant/LDS mixture per on a gel using standard Western blot techniques.

963

964 The Western blot intensities were obtained by measuring the chemiluminescence counts per
965 mm² (I = count/mm²). The obtained intensities were plotted in GraphPad Prism for melt
966 curves, with the luminescence count normalized to the control count at 37 °C. The IsoT C–R
967 data was analyzed and normalized to the maximum compound concentration. The normalized
968 intensities were plotted and analyzed using GraphPad Prism. Data points are shown as mean
969 values with error bars indicating the standard error of the mean. Concentration–response
970 curves were fitted using the modified logistic Hill equation algorithm included in the
971 GraphPad Prism software. The obtained CETSA™ EC₅₀ concentration response values
972 represent the half maximal concentration of the ligands for stabilizing hFEN1 at 50 °C. The
973 quoted EC₅₀ with 95% confidence intervals is therefore a relative measure of target
974 engagement of compound available for interaction with FEN1 in intact SW-620 cells.

975

976 **Cytotoxicity Assay** – SW620 cells were obtained from ATCC and HeLa SilenciX cell lines
977 stably expressing shRNA against *Fen1*, *Rad54b* or a non-targeting control were obtained from
978 Tebu Biosciences. Cell-line identity was confirmed by short tandem repeat fingerprinting prior
979 to banking and cells are routinely tested for mycoplasma contamination. SilenciX gene
980 knockdown was confirmed by quantitative PCR. Exponentially growing cells were split into

981 6-well plates at an appropriate density in Dulbecco's Modified Eagle's Medium (DMEM)
982 supplemented with 2 mM L-glutamine and 10% foetal calf serum (FCS) and incubated for 24
983 h to allow cells to adhere. Cells were treated with compound **1** or **4** (diluted from DMSO
984 stock solution) at the concentration stated. For the MMS sensitivity assay, cells were pre-
985 treated with 100 μ M MMS in DMEM for 2 h before replacing the media with DMEM
986 containing the stated concentration of **1** or **4**. For siRNA survival assays, *Fen1* knockdown
987 was achieved by treating with targeting and non-targeting siRNA pools (Dharmacon) for 24 h
988 using RNAiMAX lipofectamine transfection reagent (Life Technologies) before cells were
989 allowed to recover in fresh media. In all cases, plates were incubated for 10–14 days to allow
990 for colony formation. Colonies were stained with crystal violet and colony frequencies
991 determined using the GelCount automated system (Oxford Optronix). Survival is expressed as
992 a percentage of a mock-treated control. Knockdown of *Fen1* by siRNA was confirmed by
993 Western blot.

994

995 ***DNA Damage Induction Assay*** – Exponentially growing SW620 cells were seeded in 6-well
996 plates and incubated for 4 days with compound **1** at the stated dose. Cells were subsequently
997 washed, trypsinized and lysed in Cell Panel Lysis Buffer (5 mM Tris-HCl, 3 mM EDTA, 3
998 mM EGTA, 50 mM NaF, 2 mM sodium orthovanadate, 0.27 M sucrose, 10 mM β -
999 glycerophosphate, 5 mM sodium pyrophosphate, and 0.5% Triton X-100) supplemented with
1000 complete protease and phosSTOP phosphatase inhibitors (both Roche). Proteins were
1001 separated by gel electrophoresis and transferred to nitrocellulose membrane by Western blot.
1002 Membranes were probed, at a concentration of 1:1000 unless stated otherwise, for cleaved
1003 PARP (#9541, Cell Signaling Technology), γ H2AX (#2577, Cell Signaling Technology;
1004 1:500), GAPDH (#3683, Cell Signaling Technology; 1:5000), FEN1 (ab109132, Abcam),
1005 phospho-ATM (Ser1981) (ab81292, Abcam), PARP (51-6639GR, BD Biosciences), ATM
1006 (sc-23921, Santa Cruz Biotechnology) and FANCD2 (sc-20022, Santa Cruz Biotechnology).

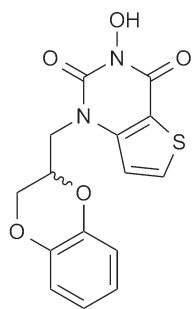
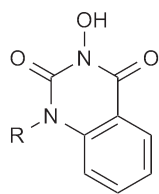
1007

1008 **Accession Codes** – The PDB accession code for the X-ray crystal structure of compound **1**
1009 bound to human FEN1, as detailed above, is 5FV7.

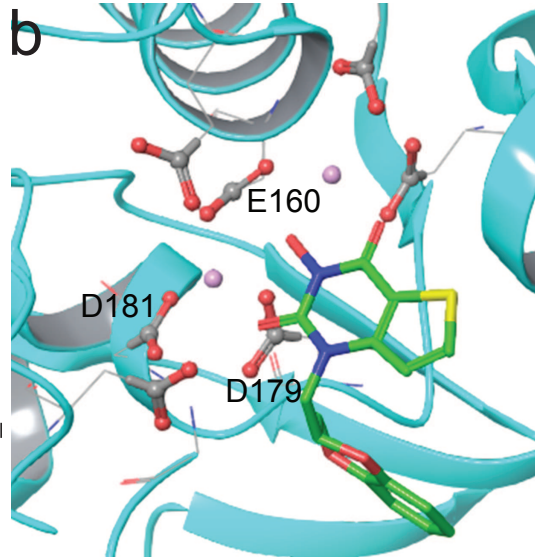
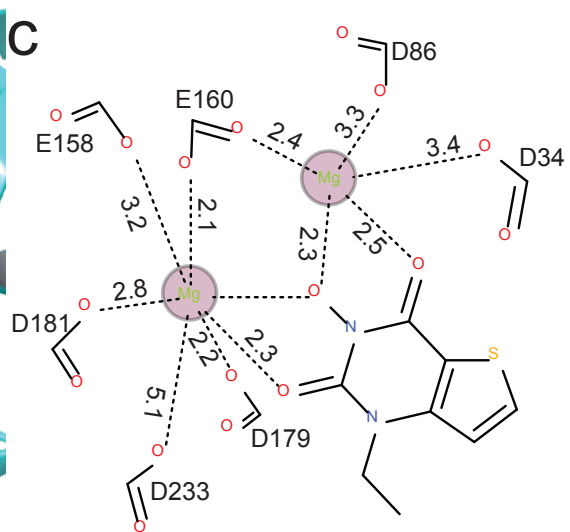
1010

1011 **Additional References for Methods**

- 1012 48 Eschenfeldt, W. H. *et al.* Cleavable C-terminal His-tag vectors for structure
1013 determination. *J. Struct. Funct. Genom.* **11**, 31-39, doi:10.1007/s10969-010-9082-y
1014 (2010).
- 1015 49 Studier, F. W. Protein production by auto-induction in high-density shaking cultures.
1016 *Protein Express. Purif.* **41**, 207-234, doi:10.1016/j.pep.2005.01.016 (2005).
- 1017 50 Fien, K. & Stillman, B. Identification of replication factor C from *Saccharomyces*
1018 *cerevisiae*: a component of the leading-strand DNA replication complex. *Mol. Cell*
1019 *Biol.* **12**, 155-163, doi:10.1128/mcb.12.1.155 (1992).
- 1020 51 Chang, J. H., Xiang, S., Xiang, K., Manley, J. L. & Tong, L. Structural and
1021 biochemical studies of the 5'→3' exoribonuclease Xrn1. *Nat. Struct. Mol. Biol.* **18**,
1022 270-276, doi:10.1038/nmsb.1984 (2011).
- 1023 52 Collaborative Computational Project Number 4. The CCP4 suite: programs for
1024 protein crystallography. *Acta Crystallogr. D Biol. Crystallogr.* **50**, 760-763,
1025 doi:10.1107/S0907444994003112 (1994).
- 1026 53 Emsley, P., Lohkamp, B., Scott, W. G. & Cowtan, K. Features and development of
1027 Coot. *Acta Crystallogr. D Biol. Crystallogr.* **66**, 486-501,
1028 doi:10.1107/S0907444910007493 (2010).
- 1029 54 Buster version 2.11.2. (Global Phasing Ltd., Cambridge, United Kingdom, 2011).
- 1030 55 Keller, S. *et al.* High-precision isothermal titration calorimetry with automated peak-
1031 shape analysis. *Anal. Chem.* **84**, 5066-5073, doi:10.1021/ac3007522 (2012).
- 1032 56 Houtman, J. C. D. *et al.* Studying multisite binary and ternary protein interactions by
1033 global analysis of isothermal titration calorimetry data in SEDPHAT: Application to
1034 adaptor protein complexes in cell signaling. *Protein Sci.* **16**, 30-42,
1035 doi:10.1110/ps.062558507 (2007).
- 1036 57 Izumi, T. & Mitra, S. Deletion analysis of human AP-endonuclease: minimum
1037 sequence required for the endonuclease activity. *Carcinogenesis* **19**, 525-527,
1038 doi:10.1093/carcin/19.3.525 (1998).
- 1039 58 Clegg, R. M. *et al.* Fluorescence resonance energy transfer analysis of the structure of
1040 the four-way DNA junction. *Biochemistry* **31**, 4846-4856, doi:10.1021/bi00135a016
1041 (1992).
- 1042

a**1**

- 2 R = cyclopropylmethyl
- 3 R = H
- 4 R = 4-methoxybenzyl

b**c****d**